

Detection of Pulsatile Oscillations via Ultrasound Localization Microscopy

Luca Giaccone

*Dept. of Information Engineering
and Computer Science
University of Trento
Trento, Italy
0009-0001-8432-367X*

Giulia Tuccio

*Dept. of Information Engineering
and Computer Science
University of Trento
Trento, Italy
0000-0001-5419-5892*

Libertario Demi

*Dept. of Information Engineering
and Computer Science
University of Trento
Trento, Italy
0000-0002-0635-2133*

Abstract—Ultrasound localization microscopy (ULM) provides angle independent velocity measurements in vascular networks with sub-wavelength resolution, offering a potential alternative to conventional ecodoppler velocity estimation currently used in clinical practice. However, this increased sensitivity also makes the measurements noisier and more difficult to interpret, due to error accumulation across multiple steps of the ULM pipeline. To enhance interpretability, we propose to use physics-informed flow modeling to constrain and clarify velocity estimates. While the steady Poiseuille flow model is widely adopted, such approximation may fail to capture the vascular dynamics. In this study, we show that ULM is sensitive enough to resolve pulsatile flow oscillations. We evaluate six fluid dynamics models on *in vitro* data and show that considering pulsatility and slip boundary conditions lead to a more robust representation of the flow dynamics beyond noise.

Index Terms—Ultrasound localization microscopy, pulsatile flow, dynamic velocity modeling

I. INTRODUCTION

Many studies [1]–[5] have shown that ultrasound localization microscopy represents an effective tool for microvasculature imaging. ULM tracks microbubbles (MBs) injected into the bloodstream, with the key advantage of estimating velocities at the micrometric scale. However, the interpretation of these velocities has been limited by measurement noise, tracking errors and the intrinsic complexity of fluid dynamics.

To address some of these limitations, recent works [6]–[10] introduced Dynamic ULM (DULM). By contextualizing ULM measurements within the cardiac cycle, DULM showed that time-resolved analysis highlight flow characteristics otherwise hidden in static, time-averaged representations. However, DULM focused only on the mean velocity in each vessel, neglecting the spatial structure of the flow.

In this study, we extend the analysis to investigate the temporal evolution of the whole radial velocity profile. Using a simple *in vitro* setup, we fit fluid dynamics flow models of increasing complexity to the measured ULM velocities. This approach allows to extract meaningful spatiotemporal flow patterns from noisy measurements and to evaluate how different physical assumptions, such as slip at the boundaries or pulsatile flow components, reflect the underlying flow dynamics.

II. METHODS

A. Data acquisition and peristaltic cycle detection

We designed an *in vitro* experiment in which a flow of lipid-coated MBs suspended in water was injected into a cylindrical tube by a peristaltic pump. ULM images of the longitudinal section of the tube were generated applying SVD filtering for denoising, gaussian fit for localization and Kalman filter for tracking. We accumulated over 7000 tracks across 30 acquisitions, as shown in Fig 1, resulting in a dataset of velocities $\{u(x_i, y_i, t_i)\}^a$, with $a \in [1, 30]$ and i indexing MBs. Tube centerline was manually segmented, allowing to compute a radial coordinate for each MB. Then we focused on the radial velocity profile, considering the datasets $\mathcal{D}_a = \{u(r_i, t_i)\}$.

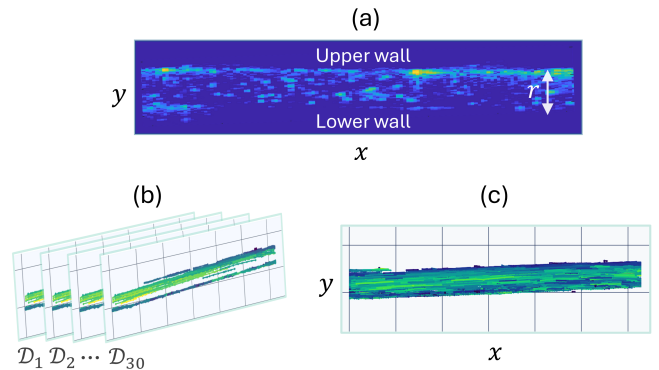


Fig. 1. Experimental setup and acquired data: (a) B-mode view of the longitudinal section of the tube, (b) ULM images generated for each acquisition, (c) accumulated MB tracks across all acquisitions.

To characterize the temporal dynamics of the flow, we computed the spatially averaged velocity for each acquisition

$$\bar{u}(t)_a = \frac{1}{N_t^{(a)}} \sum_{i \in \mathcal{D}_a | t_i=t} u(r_i, t_i), \quad (1)$$

where $N_t^{(a)}$ is the number of sampled velocities at time t in acquisition a . As expected, $\bar{u}(t)$ exhibited clear periodicity as shown in Fig. 2. We detected the outer minima of $\bar{u}(t)$ and we used them as reset points, defining $t = 0$ at the beginning of each peristaltic cycle. By aligning all velocity

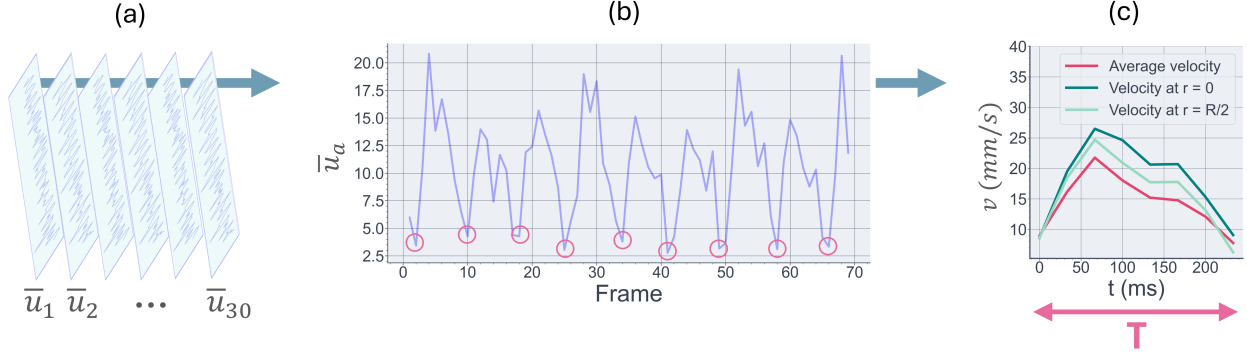


Fig. 2. Data synchronization pipeline: (a) for each acquisition the averaged velocity $\bar{u}(t)_a$ is computed, (b) outer local minima (red markers) are used as reset points to set the start of a peristaltic cycle, (c) velocity measurements are synchronized within a single time period T .

measurements relative to their corresponding peristaltic cycles, we synchronized data within each acquisition and then across all acquisitions. This allowed to obtain a unified dataset of velocities $\mathcal{D} = \{u(r_i, t_i)\}$, with $t_i \in [0, T]$. This synchronized dataset was then used for fitting fluid dynamics models.

B. Fluid dynamics models

The motion of a viscous incompressible fluid in a circular pipe of radius R is governed by the Navier–Stokes equations [11]. In cylindrical coordinates (r, θ, z) , assuming flow only in the z -direction, the latter reduces to

$$\frac{\partial u}{\partial t} = -\frac{1}{\rho} \frac{\partial p}{\partial z} + \frac{\mu}{\rho} \left(\frac{\partial^2 u}{\partial r^2} + \frac{1}{r} \frac{\partial u}{\partial r} \right), \quad (2)$$

where $u = u(r, t)$ is the axial velocity, ρ is the fluid density, μ is the dynamic viscosity and $p = p(z, t)$ is the pressure. Assuming a steady flow driven by a constant pressure gradient

$$\frac{\partial p}{\partial z} = -P \quad (3)$$

equation (2) can be integrated imposing slip boundary condition at the pipe walls

$$u(R) = u_s \quad (4)$$

giving a steady analytical solution [13] for the velocity profile

$$u_P(r) = u_{max} \left(1 - \frac{r^2}{R^2 + 2RL_s} \right), \quad (5)$$

where $L_s = 2\mu u_s / RP$ is the so-called slip length. Note that, for $u_s \rightarrow 0$ we recover the classical no-slip Poiseuille solution.

However, flow in the vasculature is highly unsteady. Womersley [12] studied the solution of (2) in the presence of a time-periodic pressure gradient

$$\frac{\partial p}{\partial z} = -c e^{i\omega t}, \quad (6)$$

where c is an amplitude coefficient and ω is the pulse frequency. In this case, the solution is

$$u_W(r, t) = \frac{R^2}{\mu} \Re \left\{ \frac{ic}{\alpha^2} \left[1 - \frac{J_0(i^{3/2} \alpha \frac{r}{R})}{J_0(i^{3/2} \alpha)} \right] e^{i\omega t} \right\}, \quad (7)$$

where J_0 is the Bessel function and $\alpha = R(\rho \omega / \mu)^{1/2}$ is the dimensionless Womersley number.

Finally, thanks to the linearity of (2), the solution for a general periodic pressure gradient of the form

$$\frac{\partial p}{\partial z} = -P - \sum_k c_k e^{i\omega_k t} \quad (8)$$

can be written as a superposition of (5) and (7)

$$u(r, t) = u_P(r) + \sum_k u_W^{(k)}(r, t), \quad (9)$$

where each term $u_W^{(k)}(r, t)$ corresponds to a Womersley's response to the k -th harmonic component of the pressure signal.

C. Models fitting

In this study we considered three models for the pressure gradient driving the flow

$$\frac{\partial p}{\partial z} = -P, \quad (10)$$

$$\frac{\partial p}{\partial z} = -P - c e^{i\omega t}, \quad (11)$$

$$\frac{\partial p}{\partial z} = -P - \sum_{k \in \{1, 2\}} c_k e^{i\omega_k t}. \quad (12)$$

Each of these was evaluated under both no-slip and slip boundary conditions, resulting in a total of six velocity models for comparison.

The steady solution (5) depends on parameters $\Theta_P = [u_{max}, L_s, R]$, where R was fixed to the maximum measured radial coordinate. For the no-slip case, we set $L_s = 0$ and fitted only u_{max} , otherwise both u_{max} and L_s were estimated. Each Womersley solution of the form (7) involves parameters $\Theta_W = [R, \mu, c, \rho, \omega]$. As before, we fixed R to

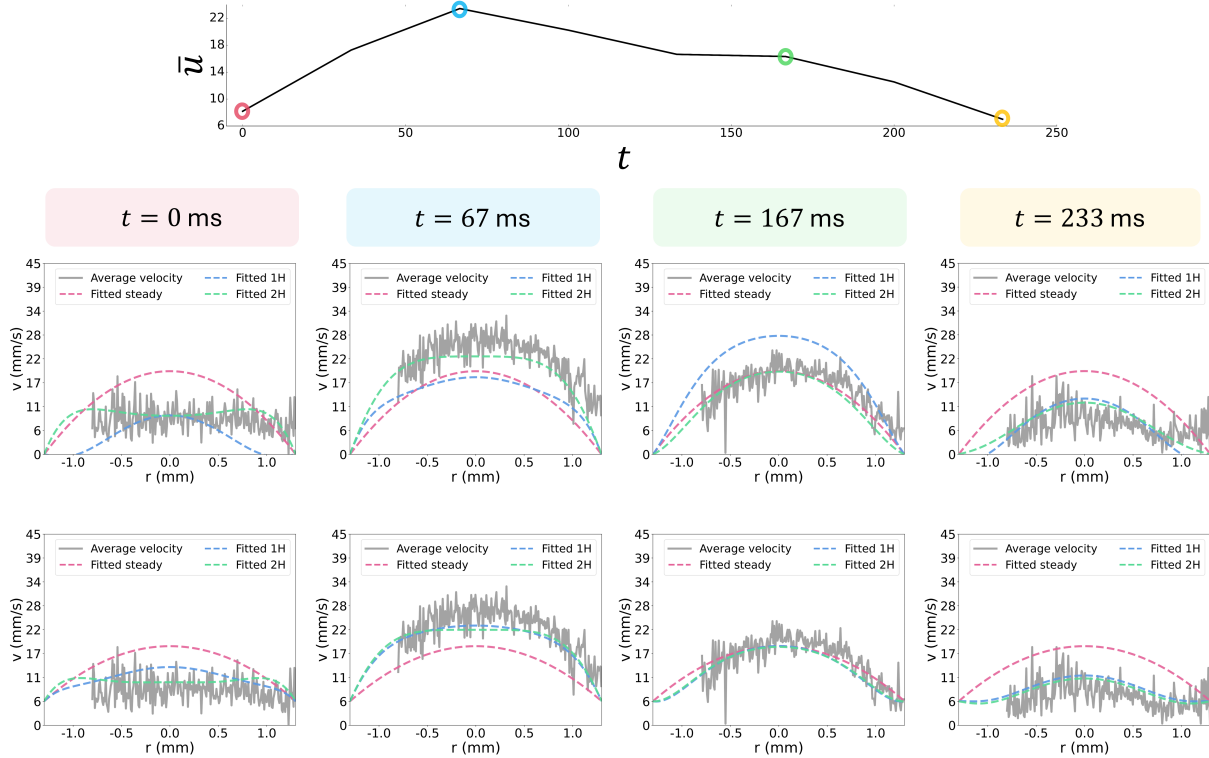


Fig. 3. Comparison between measured radial velocity profiles and model predictions. Columns display velocity profiles at four different times within the peristaltic cycle, whereas first and second rows respectively consider no-slip and slip boundary conditions.

the maximum measured radius and we set $\rho = 10^3 \text{ kg/m}^3$ and $\mu = 10^{-3} \text{ Pas}$, consistent with the physical properties of water. Therefore, for each Womersley's term we fitted only two parameters: c and ω . We studied the Fourier spectrum of the measured average velocity $\bar{u}(t)$, which revealed two dominant frequency components $[\omega_1, \omega_2]$ associated with the peristaltic pulse. These were used as initial guesses for the frequencies in the fitting process. Model parameters were estimated using a least-squares approach, by minimizing the residual

$$\text{res} = \sum_{i \in \mathcal{D}} (u_i - \hat{u}_i)^2, \quad (13)$$

where $u_i = u(r_i, t_i)$ denote the measured velocity and $\hat{u}_i = u_{\text{model}}(r_i, t_i)$ the corresponding predicted value.

D. Models evaluation

To quantitatively compare the performance of different models, we employed a set of standard error metrics computed over the entire synchronized dataset $\mathcal{D} = \{u(r_i, t_i)\}$. The following evaluation metrics were used:

- **Root Mean Squared Error (RMSE):** Measures the square root of the average squared difference between predicted and measured velocities. It penalizes larger errors more heavily than smaller ones:

$$\text{RMSE} = \sqrt{\frac{1}{N} \sum_{i=1}^N (u_i - \hat{u}_i)^2}.$$

- **Mean Absolute Error (MAE):** Computes the average of the absolute differences between predicted and measured velocities. It provides a more direct interpretation of the average error magnitude:

$$\text{MAE} = \frac{1}{N} \sum_{i=1}^N |u_i - \hat{u}_i|.$$

- **Relative RMSE:** Normalizes the RMSE by the velocity range, defined as $v_{\text{range}} = \max_i u_i - \min_i u_i$, to scale the error on dataset dynamics:

$$\text{Relative RMSE} = \frac{\text{RMSE}}{v_{\text{range}}}.$$

- **Relative MAE:** As with RMSE, the MAE is normalized by the velocity range:

$$\text{Relative MAE} = \frac{\text{MAE}}{v_{\text{range}}}.$$

- **Coefficient of Determination (R^2):** Measures the proportion of the variance in the measured velocities that is captured by the model. A value of $R^2 = 1$ indicates perfect prediction, while $R^2 = 0$ corresponds to a model that does no better than the mean of the data:

$$R^2 = 1 - \frac{\sum_{i=1}^N (u_i - \hat{u}_i)^2}{\sum_{i=1}^N (u_i - \bar{u})^2},$$

where $\bar{u} = \frac{1}{N} \sum_{i=1}^N u_i$ is the total mean of the measured velocities.

TABLE I

	Poiseuille	Womersley 1w	Womersley 2w	Poiseuille slip	Womersley 1w slip	Womersley 2w slip
RMSE	9.382×10^{-3}	8.139×10^{-3}	7.920×10^{-3}	9.231×10^{-3}	7.963×10^{-3}	7.735×10^{-3}
MAE	7.514×10^{-3}	6.205×10^{-3}	5.966×10^{-3}	7.408×10^{-3}	6.074×10^{-3}	5.809×10^{-3}
RMSE (% of range)	16.99	14.74	14.34	16.71	14.42	14.00
MAE (% of range)	13.60	11.23	10.80	13.41	11.00	10.52
R^2	0.07	0.30	0.34	0.10	0.33	0.37

III. RESULTS

Figure 3 shows the fitted velocity profiles compared to the measured radial velocity at four representative time instants within a peristaltic cycle. The experimental data were binned over a fine partition of the interval $[-R, R]$ and averaged to facilitate visual comparison. During data acquisition and ULM processing, we observed significant disturbances near the upper region of the tube, where MBs tended to aggregate and adhere to the wall, resulting in high measurement uncertainty. To ensure data reliability, we excluded measurements with $r < -0.8$ mm from the analysis. The first row of Figure 3 presents the results for the steady, single-frequency, and two-frequency unsteady models assuming no-slip boundary conditions. The second row shows the corresponding fits for models allowing slip at the wall.

Table I summarizes the evaluation metrics introduced in Section II-D for all six models. Across all metrics, the two-frequency model with slip boundary condition consistently achieves the best performance.

IV. DISCUSSION AND CONCLUSION

Our modeling approach captures the most notable qualitative features of the velocity measurements. In particular, the non-zero velocity observed at the vessel wall and the dynamic evolution of the radial velocity profile throughout the peristaltic cycle. This result is consistent with the physical expectation that the classical no-slip condition may not hold in flows formed by discrete MBs, which do not behave as a continuous fluid.

Although increasing model complexity results in RMSE and MAE improvements, these gains are smaller than how we expected. This can be explained by the high variability of ULM velocity measurements (see Fig. 3). Yet it is unlikely that the flow exhibits such complex velocity fluctuations, rather, the observed variability may arises from measurement noise, errors in the ULM processing pipeline, and the complex motion and interaction of MBs. This highlights again a key challenge in interpreting ULM data: the necessity of developing robust analysis tools that simplify the noisy datasets and extract the underlying physically meaningful flow information. A similar pattern is observed in the coefficient of determination R^2 , where dynamic models show a more noticeable improvement. Specifically, the two-harmonic slip model achieves approximately a 30% increase in R^2 compared to the steady Poiseuille model, although the best R^2 remains just above 0.4. However, it is important to note that achieving $R^2 = 1$ would imply

perfectly fitting all the variance in the data, including noise and measurement errors, which would mean overfitting the signal.

Overall, this study shows that incorporating dynamic analysis with more sophisticated physical flow models can enhance the interpretation of ULM velocity measurements. This approach move the first steps towards more accurate and physically grounded assessments of ULM flow estimation.

REFERENCES

- [1] Song P, Rubin JM, Lowerison MR. Super-resolution ultrasound microvascular imaging: Is it ready for clinical use? *Z Med Phys.* 2023 Aug.
- [2] Dencks S, Lowerison M, Hansen-Shearer J, Shin Y, Schmitz G, Song P, Tang MX. Super-Resolution Ultrasound: From Data Acquisition and Motion Correction to Localization, Tracking, and Evaluation. *IEEE Trans Ultrason Ferroelectr Freq Control.* 2025 Apr.
- [3] Erico, C., Pierre, J., Pezet, S. et al. Ultrafast ultrasound localization microscopy for deep super-resolution vascular imaging. *Nature* 527, 499–502 (2015).
- [4] O. Couture, V. Hingot, B. Heiles, P. Muleki-Seya and M. Tanter, "Ultrasound Localization Microscopy and Super-Resolution: A State of the Art," in *IEEE Transactions on Ultrasonics, Ferroelectrics, and Frequency Control*, vol. 65, no. 8, pp. 1304-1320, Aug. 2018.
- [5] Yi HM, Lowerison MR, Song PF, Zhang W. A Review of Clinical Applications for Super-resolution Ultrasound Localization Microscopy. *Curr Med Sci.* 2022 Feb.
- [6] Bourquin C, Poree J, Lesage F, Provost J. In Vivo Pulsatility Measurement of Cerebral Microcirculation in Rodents Using Dynamic Ultrasound Localization Microscopy. *IEEE Trans Med Imaging.* 2022 Apr.
- [7] Bourquin C, Porée J, Rauby B, Perrot V, Ghigo N, Belgharbi H, Bélanger S, Ramos-Palacios G, Cortes N, Ladret H, Ikan L, Casanova C, Lesage F, Provost J. Quantitative pulsatility measurements using 3D dynamic ultrasound localization microscopy. *Phys Med Biol.* 2024 Feb.
- [8] Cormier P, Poree J, Bourquin C, Provost J. Dynamic Myocardial Ultrasound Localization Angiography. *IEEE Trans Med Imaging.* 2021 Dec.
- [9] Ghigo N, Ramos-Palacios G, Bourquin C, Xing P, Wu A, Cortés N, Ladret H, Ikan L, Casanova C, Porée J, Sadikot A, Provost J. Dynamic Ultrasound Localization Microscopy Without ECG-Gating. *Ultrasound Med Biol.* 2024 Sep.
- [10] Xing P, Perrot V, Dominguez-Vargas AU, Porée J, Quessy S, Dancause N, Provost J. 3D ultrasound localization microscopy of the nonhuman primate brain. *EBioMedicine.* 2025 Jan.
- [11] Drazin PG, Riley N. *The Navier-Stokes Equations: A Classification of Flows and Exact Solutions.* Cambridge University Press; 2006, pp 128-129.
- [12] Womersley JR. Method for the calculation of velocity, rate of flow and viscous drag in arteries when the pressure gradient is known. *J Physiol.* 1955 Mar 28.
- [13] Cox, B.J., Hill, J.M. Flow through a circular tube with a permeable Navier slip boundary. *Nanoscale Res Lett* 6, 389 (2011).